

Polarization Corrected Temperatures for 10-, 19-, 37-, and 89-GHz Passive Microwave Frequencies

Daniel J. Cecil¹ and Themis Chronis²

¹ NASA George C. Marshall Space Flight Center, Huntsville, AL.

² University of Alabama in Huntsville.

Submitted to:

Journal of Applied Meteorology and Climatology

January 2018, Revised May 2018

Corresponding author email:

Daniel.J.Cecil@nasa.gov

Abstract

Coefficients are derived for computing polarization corrected temperature (PCT) for 10-, 19-, 37- and 89-GHz (and similar) frequencies, with applicability to satellites in the Global Precipitation Measurement mission constellation and their predecessors. PCT for 10- and 19-GHz frequencies have been non-existent or seldom used in the past; developing those is the main goal of this study. For 37-GHz and 89-GHz, other formulations of PCT have already become well established. We consider those frequencies here in order to test whether the large sample sizes that are readily available now would point to different formulations of PCT.

The purpose of the PCT is to reduce effects of surface emissivity differences in a scene, and draw attention to ice scattering signals related to precipitation. In particular, our intention is to develop PCT formula that minimize differences between land and water surfaces, so that signatures resulting from deep convection are not easily confused with water surfaces. The new formulations of PCT for 10- and 19-GHz measurements hold promise for identifying and investigating intense convection. Four examples are shown from relevant cases. The PCT for each frequency is effective at drawing attention to the most intense convection, and removing ambiguous signals that are related to underlying land or water surfaces. For 37-GHz and 89-GHz, the older formulations of PCT from the literature yield generally similar values as ours, with the differences mainly being a few K over oceans. An optimal formulation of PCT can depend on location and season; results are presented here separated by latitude and month.

1. Introduction

Satellite-borne passive microwave imagers provide information on the characteristics of the Earth's surface, its overlying atmosphere, and precipitation. Warm brightness temperatures can result from high emissivity land surfaces or from emission by liquid cloud or rain hydrometeors aloft. Low brightness temperatures can result from low emissivity surfaces such as ice and water bodies, or from scattering by large precipitation ice particles. Interpretation of the cause of a low brightness temperature can be ambiguous because it could result from scattering by graupel or hail in a convective storm, or from a wet or water-covered surface. The interpretation is especially difficult when an over-land scene includes convective storms, inland water bodies, and potentially even floodwater or wet soil from recent precipitation (Fig. 1). This paper aims to enable more straightforward assessment of the impacts of hydrometeors on passive microwave measurements, by minimizing effects due to variability in the underlying surface.

An example of the ambiguity in discriminating storms from surface conditions is shown in Fig. 1. Strong convective storms are depicted by radar in Fig. 1a, and some of them produce lower brightness temperatures than the adjacent land scenes in Fig. 1b-d, especially in the 37-GHz channel (and in higher frequencies, which are not shown here). For the lower frequencies, most of the storm-associated brightness temperatures are no lower than the precipitation-free brightness temperatures over the nearby Gulf of Mexico (lower right portion of each panel). Over the eastern part of Texas, there are several small areas with reduced brightness temperatures that do not correspond to storms in the radar image. Instead, they are associated with lakes.

Most current imagers have separate horizontally polarized and vertically polarized channels for most frequencies, particularly for frequencies near 10-, 19-, 37-, and 89-GHz. Large polarization differences in the upwelling brightness temperatures typically result from water surfaces and surfaces with high soil moisture. Scattering by large ice hydrometeors typically leads to much smaller polarization differences. Dry land surfaces also have smaller polarization differences. A linear combination of horizontally polarized and vertically polarized brightness temperatures, termed polarization corrected temperature (PCT), can remove much of the effect from varying land surface characteristics (Weinman and Guetter 1977; Grody 1984; Spencer et al. 1989; Barrett and Kidd 1990; Todd and Bailey 1995; Kidd 1998; Toracinta et al. 2002). The PCT is then useful for identifying scenes with precipitation, with less ambiguity related to the underlying surface type or surface conditions. Formulae for PCT have been presented in various forms in the literature, but here we follow the form:

$$PCT_f = (1 + \Theta_f) TB_{fv} - \Theta_f TB_{fh} \quad (1)$$

where Θ is a coefficient that minimizes effects of surface emissivity and TB is the brightness temperature at frequency f and polarization v (vertical) or h (horizontal).

Spatial resolution and sensitivity to typical graupel sizes both increase with increasing frequency (decreasing wavelength) of the radiation. As such, much of the work involving passive microwave PCT has focused on channels in the 85-91-GHz range, with some attention also given to channels near 37-GHz. The Spencer et al. (1989) PCT_{85} is probably the most widely used today, with the coefficient $\Theta_{85}=0.818$ derived from several days of Special Sensor Microwave Imager (SSM/I; Hollinger et al. 1990) global observations of cloud-free oceanic areas. Before settling on this value for Θ_{85} , Spencer et al. (1989) also discussed model calculations that imply values in the range of 0.54-0.61, but those values did not work well with the observed SSM/I data. The Spencer

et al. (1989) formula was subsequently used in databases of mesoscale convective systems (Mohr and Zipser 1996) and more general precipitation features (Nesbitt et al. 2000; Liu et al. 2008), and numerous related studies.

Although Spencer et al. (1989) identified a constant Θ_{85} value in order to apply a uniform standard for global analysis, others have emphasized that optimal choices of Θ_{85} can be a function of location, season, and local conditions. Barrett and Kidd (1990) proposed $\Theta_{85}=0.64$ for northwestern Europe and the United Kingdom during summer and autumn. Todd and Bailey (1995) and Kidd (1998) empirically derived Θ_{85} values separately for each scene (each SSMI overpass of the United Kingdom), allowing Θ_{85} to vary from day to day. Their Θ_{85} values generally ranged from about 0.5-0.75. Kidd (1998) showed large daily and intra-day variations superimposed on an apparent annual cycle for Θ_{85} , with lowest values in winter and highest values in summer. Todd and Bailey (1995) and Kidd (1998) argued that allowing Θ_{85} to vary with local conditions is important for distinguishing light rain from rain-free regions.

Before the first SSMI was launched with its 85-GHz frequency in 1987, 37-GHz measurements were used from the Nimbus-6 Electrically Scanning Microwave Radiometer (ESMR) and Scanning Multichannel Microwave Radiometer (SMMR). Weinman and Guetter (1977) developed a linear transformation (they did not use the term PCT) for use with ESMR. Their equation 16 uses $\Theta_{37}=1.2$ based on theory and $\Theta_{37}=1.5$ based empirically on ESMR observations. Grody (1984) derived $\Theta_{37}=1.08$ and $\Theta_{19}=1.38$ for SMMR. Toracinta et al. (2002) used $\Theta_{37}=1.2$ for the Tropical Rainfall Measuring Mission (TRMM; Kummerow et al. 1998) precipitation feature database (Liu et al. 2008), using TRMM Microwave Imager (TMI) data. That value continues to be used for Global Precipitation Measurement (GPM; Hou et al. 2014) mission precipitation features. Lee et al. (2002) used $\Theta_{37}=1.18$, and that value continues to be used for the

popular Naval Research Laboratory – Monterey Tropical Cyclone Webpage. Jiang et al. (2018) provide a nice discussion of PCT_{37} , and use it to interpret precipitation types in tropical cyclones.

Precipitation estimation, and more specifically the discrimination between raining and non-raining areas, motivated much of the aforementioned research involving PCT_{85} . Cecil et al. (2005) and Zipser et al. (2006) emphasized the use of PCT_{37} in studies of intense thunderstorms, using TRMM measurements. Cecil (2009) empirically related TRMM PCT_{85} and PCT_{37} to reports of large hail reaching the surface, and Cecil and Blankenship (2012) applied the PCT_{37} -hail relationship to Advanced Microwave Scanning Radiometer for Earth Observing System (AMSR-E) PCT_{36} (using the same Θ_{37} as in Toracinta et al. 2002) in order to estimate a global climatology of hailstorm occurrence. Cecil (2009) also noted that 19-GHz measurements from TRMM are more effective at giving a high-confidence indication of large hail, although relatively coarse spatial resolution and the lack of a well-established PCT_{19} made it more difficult to use. Mroz et al. (2017) tested an early version of the PCT_{19} that is presented here, and found it to be more effective for identifying hail than any of the other GMI frequencies. We did not have a version of PCT_{10} ready for inclusion in the Mroz et al. study, but even without applying the PCT, the low-resolution 10-GHz measurements did show some usefulness in that study.

This paper is motivated by observations of reduced brightness temperatures in TRMM and GPM 19-GHz and 10-GHz channels for some intense thunderstorms, besides the reduced brightness temperatures that have already been well documented for the 85-89-GHz and 36-37-GHz frequencies. Systematic analysis of thunderstorm-related signatures in the 19-GHz and 10-GHz channels is difficult without first applying a PCT transformation to those channels. This paper empirically derives values for Θ_{10} , Θ_{19} , Θ_{37} , and Θ_{89} from three years of GPM measurements, and considers their spatial and seasonal variability. The main goal is to derive and evaluate useful

coefficients for PCT_{10} and PCT_{19} , since those have rarely been used in the past. The values for Θ_{37} and Θ_{89} from the literature have proven effective over the years. We re-examine them here because it has become convenient to apply our methods to vastly larger sample sizes than were used in the previous studies. Our optimal coefficients (producing the smallest contrast between land and water surfaces, and thus less ambiguity related to surface type) for PCT_{37} and PCT_{89} are slightly different from those that have already been widely used. Our analysis shows that a broad range of coefficient values can be defensible for these frequencies, when applied to global studies. As such, there may be little practical benefit for many users to switch from the previous Θ_{37} and Θ_{89} values to our marginally more effective values. The values derived for Θ_{10} and Θ_{19} do show promise for enabling improved analysis of vigorous, deep convection.

2. Data and Methods

GPM Microwave Imager (GMI) version V05A brightness temperatures (GPM Science Team, 2016) from 1 April 2014 – 31 March 2017 are used for development of PCT coefficients in this study. Every other GPM orbit (odd-numbered orbits from 503-17553) and every tenth scan position (of the 221 positions per GMI scan) are used, in order to speed up the required processing. This amounts to using 5% of the available data during a 3-year period, while still sampling a broad variety of conditions.

The GMI Level 2 (“GPROF”) files (Iguchi and Meneghini, 2016) are further used to identify precipitation-free pixels, and to classify each pixel as land (GPROF surface types 3-5, corresponding to “maximum vegetation”, “high vegetation”, and “moderate vegetation”) or ocean (GPROF surface type 1). The “ocean” classification can include large water bodies, for example

the Great Lakes. Sea ice, arid regions, surface snow cover, rivers, coasts, and precipitation scenes are excluded.

Each orbit is divided into 5° latitude bins. Statistics are derived separately for each of these bins that has at least 10 land and 10 water pixels without precipitation. Latitude bins without enough land and water pixels in a given orbit are ignored, because a comparison between land and water pixels is required for building the empirical relationships. For a given latitude bin in a given GPM orbit, candidate PCT values using a given Θ are computed for each pixel. The differences between PCT values are then computed for every possible pairing of land and water pixels within that latitude bin. If there are 10 land and 10 water pixels, for example, there would be 100 pairs with land-water PCT differences. Since the GMI swath is about 900 km wide and the satellite only takes a few minutes to traverse 5° , most of the land-water differences are computed within a few hundred km and a few minutes of each other. Ideally, a perfect choice of Θ would yield PCT differences near zero for all possible land-water pairings, and a poor choice of Θ would yield large PCT differences. That ideal scenario is not realistic, because inhomogeneities in a scene besides surface type would give non-zero differences. A histogram of PCT differences is computed from the land-water pairings, and added to histograms computed from other orbits. This process is repeated for candidate PCT values computed with Θ ranging from 0.3 to 1.79 in increments of 0.01. Each GMI frequency under consideration is treated separately, at its native resolution.

The PCT difference histograms are computed with bin size 2 K. They are accumulated separately for each 5° latitude bin, for each month of the year, and for each Θ value. Even though we considered only 5% of the available GMI data, before further restricting the data by surface type and precipitation, most latitudes (from 55° S to 60° N) and months contain tens of millions of land-water pairings for the resulting histograms. The sample size (Table 1) is relatively small

at far the southern latitudes because there is so little land there, and is large at the far northern latitudes because of both orbital geometry and the mix of land and ocean surfaces. The seasonal variation in sample size is extreme at far northern latitudes (2 million land-water pairings in January, 357 million pairings in August) because surface snow and ice cover are eliminated.

The resulting histograms of land-water PCT differences are analyzed in Section 3 to determine which Θ values most consistently yield small PCT differences. A small difference in PCT between land and water pixel pairs indicates that the surface type is not strongly influencing the PCT, and that we can use PCT to investigate precipitation hydrometeor signatures instead. Section 3a accumulates the histograms into probability density functions across all latitudes and months for a global analysis, and Section 3b examines variability by latitude and month.

PCT coefficients based on the results from Section 3 are applied to selected cases in Section 4. Those cases were observed individually by the GMI, TMI, AMSR-E, and SSMI sensors (Table 2). The GPM XCAL dataset (Berg et al. 2016; GPM Science Team 2016; GPM Science Team 2017a,b,c) is used for these, since it applies an inter-calibration among sensors, making their calibrations consistent with GMI. The XCAL brightness temperatures are referred to as GPM level 1C version 05A, with other satellites included as GPM constellation members. GPM level 1B version 05A 85-GHz data (TRMM, 2017) are also used for the TMI case, because level 1C unnecessarily sets values below 50 K as missing. AMSR-E level 2A version 3 files (Ashcroft and Wentz, 2013) from the National Snow and Ice Data Center (NSIDC) are also used for 89-GHz for the same reason.

3. Results – Optimizing PCT Coefficients

a) Global analysis

First we consider statistics from the land-water PCT differences accumulated over all months and all regions. Since a motivation for using the PCT is to eliminate the land-water differences as much as possible, Fig. 2 shows what percentage of land-water pairs have PCT differences below 2 K (thick lines) and below 10 K (thin lines) as a function of the choice of Θ value. For convenience, we will refer to the value yielding land-water PCT differences less than 2 K the most often as the “best” performing Θ in a given analysis. These are not the Θ values we ultimately recommend using. Defining the best Θ based on how rarely it produces large (> 10 K) differences would lead to Θ values 0.03-0.04 higher. Our ultimate recommendations will consider both those definitions and the regional and seasonal variability to be addressed in Section 3b.

Fig. 3 shows probability density functions of land-water PCT differences for the Θ values that yield PCT differences less than 2 K most often, and for some other Θ values from the literature. For $\Theta_{89}=0.63$, 24% of land-water pairings have PCT differences less than 2 K, another 21% have differences between 2-4 K, and 16% have differences 4-6 K. Using $\Theta_{89}=0.82$ based on Spencer et al. (1989) reduces those percentages to 18%, 17%, and 16%, respectively. The “best” performing Θ_{37} (1.10) in this global analysis yields land-water differences in PCT_{37} that are slightly larger than the differences in PCT_{89} based on using the Spencer et al. Θ_{85} . In other words, a sub-optimal choice of Θ_{89} can outperform an optimal choice of Θ_{37} . Moving to still lower frequency channels, the “best” performing Θ_{19} (1.36) and Θ_{10} (1.48) are progressively less effective at minimizing the land-water PCT differences. This decreasing effectiveness with decreasing frequency is also seen in

Fig. 2. The Toracinta et al. (2002) coefficient $\Theta_{37}=1.20$ yields land-water PCT₃₇ differences less than 2 K 14% of the time, and between 2-4 K another 14% of the time. This is comparable to $\Theta_{19}=1.36$ yielding PCT₁₉ differences less than 2 K 15% of the time, and 2-4 K 14% of the time. For $\Theta_{10}=1.48$, only 12% of land-water pairs have PCT₁₀ differences less than 2 K and 11% between 2-4 K. For this “best” choice of Θ_{10} from the global analysis, about half the land-water pairs have PCT₁₀ differences greater than 10 K. Any choice of Θ_{10} will have many situations where it is not very effective at removing the land-water contrast.

The probability density functions in Fig. 3 isolated the Θ values that gave the sharpest peaks in the 0-2 K PCT difference bins. Fig. 4 instead depicts the performance for all Θ values, in the form of two-dimensional probability density functions. The sideways V-shapes for these two-dimensional probability density functions indicate that for each frequency, there is a preferred range of Θ values where the land-water PCT differences tend to be small. Moving away from that preferred range, Θ values that are too high or too low give larger land-water PCT differences. Minimizing those land-water differences is crucial for seamlessly interpreting the precipitation characteristics across a coastline, or in a scene including small water bodies. A narrow range of Θ values gives acceptably small land-water PCT differences for the low-frequency channels, but a broad range of Θ_{89} values gives small PCT₈₉ differences.

b) Variability by latitude and month

Figures analogous to Fig. 2-4 were generated separately for each 5° latitude bin and for each month. Lower Θ values generally have better performance (i.e., less variation in PCT) in the deep tropics than at higher latitudes. At mid- and high-latitudes, higher Θ values perform better

during the warm season and lower Θ values perform better during the cold season. The Θ values that yield the highest percentage of land-water pairs with PCT differences less than 2 K are compiled as functions of latitude and month in Table 3 (89-GHz), Table 4 (37-GHz), Table 5 (19-GHz), and Table 6 (10-GHz).

Just as a range of Θ values works better for higher frequency channels than any Θ value does for lower frequency channels in Fig. 2-4, a range of Θ values also works well in the tropics, compared to higher latitudes. As an example, the effectiveness of each Θ value at reducing the land-water contrast below 2 K (thick lines) and below 10 K (thin lines) as in Fig. 2 is reproduced separately for 0°-5° N in July (Fig. 5) and for 35°-40° N in July (Fig. 6). The best-performing Θ values are lower in the tropics than in the mid-latitudes (consistent with Tables 3-6). The PCT is so much more effective at reducing the land-water contrast in the deep tropics, there is little need to find the precise Θ value that gives the best scores there. One could choose whichever Θ value is most acceptable for the mid-latitudes, and that Θ would also work well in the tropics.

4. Discussion and examples

Consideration of Figs. 2-4, analogous figures that are segregated by latitude and month, and Tables 3-6 lead to the conclusion that while no single Θ value gives an ideal PCT formulation applicable to all places and seasons, a range of Θ values can generally give credible results. Some readers may wish to use PCT formulations that are most appropriate for particular regions or seasons, and Tables 3-6 are suitable for selecting those Θ values. Others, including ourselves, will want to apply a single Θ value for each frequency globally, all through the year. The most straightforward choice would be to take the Θ values highlighted in Section 3a, but instead we

recommend some slight modifications to account for varying performance in different regions and seasons. Our recommendations (Table 7) also round the Θ values to the nearest 0.05, since Fig. 2-4 and the analysis by latitude and by month suggest that precision to the nearest 0.01 is not warranted.

The result that a high degree of precision is not warranted in selecting Θ values also suggests that the same coefficients should be appropriate for use with other passive microwave sensors, despite differences in footprint sizes or radiometer frequencies. Small variations in the frequencies used by different radiometers can lead to brightness temperature differences of a few K in rain-free regions (or several K in rain, but raining pixels are omitted from the computation of PCT coefficients) (Yang et al. 2014). If the entire analysis were repeated using an 85.5 GHz (e.g., SSMI or TMI) or 91.7 GHz (e.g., SSMI/Sounder) frequency instead of the GMI's 89.0 GHz frequency, there may be small changes in the details of Section 3, but likely no significant change in the choice of Θ . Likewise, differences in sensors' footprint sizes should have little effect, especially since the analysis is done using precipitation-free pixels.

For passive microwave channels in the range 85-GHz – 92-GHz (including SSMI, TMI, GMI, AMSR), we recommend $\Theta_{89}=0.70$. This tends more toward the higher values that work well in the mid-latitude warm seasons than the lower values that work best in the tropics, since performance of PCT_{89} in the tropics is less sensitive to the precise choice of Θ_{89} . For similar reasons, we recommend $\Theta_{37}=1.15$ for the 36-37-GHz channels on SSMI, TMI, GMI, and AMSR.

Many publications have used $\Theta_{85}=0.818$ and $\Theta_{37}=1.2$ for PCT based on Spencer et al. (1989) and Toracinta et al. (2002), particularly for studies involving TRMM and GPM precipitation feature databases (Nesbitt et al. 2000; Liu et al. 2008). Fig. 7-8 compare PCT values computed using our recommended Θ values to those computed using the Spencer et al. (1989) and

Toracinta et al. (2002) values. The differences are mostly small, which was expected because the Spencer et al. and Toracinta et al. versions have both proven effective over the years. Figures 2 and 4 show that these small changes do tend to slightly reduce the land-water contrasts when using our new versions of PCT_{89} and PCT_{37} . Since the PCT formula in Equation (1) can be re-arranged to include a term with Θ multiplying the polarization difference, our lower choices of Θ almost always lead to slightly lower PCT values. The choice of Θ has least effect where polarization differences are small (e.g., most land areas), and greatest effect where polarization differences are large (e.g., water surfaces beneath optically thin airmasses). For PCT_{89} , the differences are less than 1 K over most land areas and 1-4 K over most ocean locations. Exceptions over land are deserts and areas of snow or ice cover, where PCT_{89} tends to be 1-3 K lower using our choice of Θ_{89} . Over oceans, the largest differences (4-8 K) coincide with dry airmasses, particularly at mid- and high-latitudes. For PCT_{37} , the differences over land are again less than 1 K except for deserts and snowpacks, where the differences are 1-2 K. Over oceans, the differences are only 2-4 K, with the higher values coinciding with drier airmasses. For both frequencies, the differences are only a few tenths of a Kelvin for pixels with substantial precipitation signatures.

For 19-GHz channels (including SSMI, TMI, GMI, AMSR), we recommend $\Theta_{19}=1.40$. This is essentially the same (after rounding) as the 1.38 value used by Grody (1984), with which we were not familiar until preparing this manuscript. For channels near 10-GHz (TMI, GMI, and AMSR), we recommend $\Theta_{10}=1.50$. As with the higher frequency channels, these recommendations for the lower frequency channels are compromises that are intended to work best in both the tropics and in mid-latitude warm seasons. For the lower frequency channels, the ability to eliminate differences between land and water-covered scenes is substantially reduced compared to the higher frequency channels.

We briefly consider cases with intense convective storms that were observed by GMI, TMI, AMSR-E, and SSMI, in order to demonstrate the utility of these new PCT formulations. These cases were previously identified by Cecil (2015) as having some of the most extreme 37-GHz or 89-GHz scattering signatures for those satellites. For each example in Fig. 9-12, the left panels show vertically-polarized brightness temperatures and the right panels show PCT (using our recommended coefficients, as in Table 7).

The storms around Texas shown in Fig. 1 are re-visited in Fig. 9, a case observed by GMI on 26 May 2015. At 89-GHz (top row), the effect of the PCT is not especially noticeable for this case, other than bringing the Gulf of Mexico temperatures closer to those over land. For the 37, 19, and 10-GHz frequencies, the PCT eliminates the sharp gradient at the coast and also eliminates the signatures associated with lakes that were mentioned with Fig. 1. The individual figure panels identify the minimum brightness temperature (or PCT) for each panel. Most of these minima are associated with the strongest storm, west of Fort Worth. The minimum TB_{10v} (Fig. 9g) is a precipitation-free Gulf of Mexico scene, but PCT_{10} (Fig. 9h) is minimized over the storm, as desired.

A case over northern Argentina observed by TMI is shown in Fig. 10. The left panels have low brightness temperatures from numerous intense thunderstorms, along with low surface emissivity features such as the Parana River, Ibera Wetlands, and the Mar Chiquita salt lake. The PCT in the right panels only highlight the strong storms. Zipser et al. (2006) highlighted this case and mentioned its lowest PCT_{37} as 69 K. Its minimum PCT_{37} is higher (74 K) in Fig. 10d because of two calibrations that were applied to TMI since that paper. The update from TRMM version 7 to version 8 (now known as GPM version 5, because TRMM is treated as part of the GPM constellation) increased TB_{37V} and TB_{37H} by 2.8 K and 2.5 K, respectively, for the coldest pixel in

this case. The recalibration for consistency with GMI (known as the GPM XCAL level 1C brightness temperatures) increases TB_{37V} by 0.69 K and decreases TB_{37H} by 1.56 K for the low end of TB_{37} values, such as this. The increased $TB_{37V} - TB_{37H}$ polarization difference adds to the PCT_{37} . The change from using Toracinta et al.'s (2002) Θ_{37} coefficient (also used by Zipser et al. 2006) to ours only amounts to 0.3 K difference between the two formulations.

Typhoon Bolaven (2005) is shown in Fig. 11, as observed near the Philippines (east of Luzon) by AMSR-E on 18 Nov 2005. The use of PCT again eliminates most of the land-water contrast (with the Philippines on the far left of each panel). But the PCT also removes much of the signal from rain in the lower frequency channels. Emission by liquid rain is seen as warm brightness temperatures over ocean in the left panels, but only the scattering by large ice particles is highlighted by the PCT in the right panels.

The SSMI has coarser resolution than GMI, TMI, and AMSR-E, and lacks a 10-GHz channel, but the PCT highlights intense convection in SSMI's 19-, 37-, and 85-GHz frequencies. The "Boundary Waters Derecho" (Price and Murphy 2002) case (Fig. 12) featured an intense storm in northern Minnesota. The PCT is again effective at removing the signal associated with the lakes in this region, and drawing attention to the storm.

The cases shown in Fig. 9-12 were selected because they were known to have extremely low PCT_{37} , so they were good candidates for having substantial ice scattering signatures in the 19- and 10-GHz channels. Indeed, the GMI and TMI cases had PCT_{19} reduced from near 300 K in the surrounding areas to 159 K and 149 K, respectively, at the convective cores. Those two cases also had noticeable scattering signatures in PCT_{10} (241 K and 265 K, respectively), despite the longer wavelength and coarser resolution for this frequency (Table 2). The AMSR-E case (Typhoon Bolaven, Fig. 11) had weaker signatures in the low frequency channels (235 K PCT_{19} ; 278 K

PCT₁₀) than the GMI and TMI cases, but it also had a weaker signature at 37-GHz (113 K). It had the lowest TB_{V89} (41 K) and PCT₈₉ (41 K) of all these cases, which may result from having an extraordinarily deep vertical layer of large graupel. The SSMI case from Minnesota had PCT₁₉ reduced to 230 K, despite SSMI's coarse resolution. Another SSMI case from the same region (28 June 1998) had PCT₁₉ scattered to 217 K (not shown).

5. Conclusions

Coefficients have been derived for computing PCT for 10-, 19-, 37- and 89-GHz (and similar) frequencies from GMI and related radiometers. While coefficient values can be optimized for particular regions and seasons using Tables 3-6, we recommend the values listed in Table 7 for global applications. These result in the formulae:

$$PCT_{10} = 2.5 TB_{10v} - 1.5 TB_{10h} \quad (2)$$

$$PCT_{19} = 2.4 TB_{19v} - 1.4 TB_{19h} \quad (3)$$

$$PCT_{37} = 2.15 TB_{37v} - 1.15 TB_{37h} \quad (4)$$

$$PCT_{89} = 1.7 TB_{89v} - 0.7 TB_{89h} \quad (5)$$

These values were tested using four cases with intense convection observed separately by the GMI, TMI, AMSR-E, and SSMI sensors. The new PCT formulations eliminated much of the contrast between land and water surfaces in all four cases and for all four frequencies. The intense convection is easily recognized with PCT depressions in each case, without having surface-related characteristics contributing other ambiguous PCT depressions.

Other formulations of PCT₈₉ and PCT₃₇ have become well established. Differences between our PCT₈₉ and that from Spencer et al. (1989) and between our PCT₃₇ and that from Toracinta et al. (2002) were examined and tend to be small, especially for measurements involving

ice scattering related to precipitation. Otherwise, our PCT_{89} and PCT_{37} tend to be a few K lower than the previous formulations over the oceans. The largest differences are over relatively dry oceanic airmasses. Differences over land are usually less than 1 K, except for deserts and snow- or ice-covered regions.

The key new developments from this paper are the coefficients for computing PCT_{19} and PCT_{10} . We see these as tools for further investigating intense thunderstorms, using GPM and other satellites with related sensors. Indeed, Mroz et al. (2017) obtained higher skill scores for hail detection using a preliminary version of our PCT_{19} than the scores obtained using higher frequencies or individual polarizations. PCT_{19} and PCT_{10} essentially mask the signals that come from inland water bodies, or from coasts. They also have little sensitivity to most precipitation, but help draw attention to the most intense convection, capable of producing large amounts of hail and/or graupel that scatter the upwelling radiation in these frequencies.

6. Acknowledgments

This research is supported by NASA's Precipitation Measurement Mission Science Team NNH15ZDA001N-PMM. GPM data provided by National Aeronautics and Space Administration (NASA) and Japan Aerospace Exploration Agency (JAXA) through the Precipitation Processing System website at <http://pps.gsfc.nasa.gov/>.

7. References

- Ashcroft, P. and F. J. Wentz. 2013. *AMSR-E/Aqua L2A Global Swath Spatially-Resampled Brightness Temperatures, Version 3*. [Indicate subset used]. Boulder, Colorado USA. NASA National Snow and Ice Data Center Distributed Active Archive Center. doi: http://dx.doi.org/10.5067/AMSR-E/AE_L2A.003. [Date Accessed: 18 June 2013].
- Barrett, E.C., and C. Kidd, 1990: Rainfall monitoring by the SSM/I in middle latitudes. *5th Conf. on Sat. Meteor. Oceanog.*, London, England, Amer. Meteor. Soc., 210-214.
- Berg, W., S. Bilanow, R. Chen, S. Datta, D. Draper, H. Ebrahimi, S. Farrar, W.L. Jones, R. Kroodsma, D. McKague, V. Payne, J. Wang, T. Wilheit, and J.X. Yang, 2016: Intercalibration of the GPM microwave radiometer constellation. *J. Atmos. Ocean. Tech.*, **33**, 2639-2654.
- Cecil, D.J., S.J. Goodman, D.J. Boccippio, E.J. Zipser, and S.W. Nesbitt, 2005: Three years of TRMM precipitation features. Part I: Radar, radiometric, and lightning characteristics. *Mon. Wea. Rev.*, **133**, 543-566.
- Cecil, D. J., 2009: Passive microwave brightness temperatures as proxies for hailstorms. *J. Appl. Meteor. Clim.*, **48**, 1281-1286.
- Cecil, D.J. and C.B. Blankenship, 2012: Toward a global climatology of severe hailstorms as estimated by satellite passive microwave imagers. *J. Clim.*, **25**, 687-703.
- Cecil, D.J., 2015: Extremely low passive microwave brightness temperatures due to thunderstorms. *20th Conference on Satellite Meteorology and Oceanography*, Amer. Meteor. Soc., Phoenix, AZ.

413 GPM Science Team, 2016: GPM GMI Brightness Temperatures L1B 1.5 hours 13 km V05,
 414 Greenbelt, MD, USA, Goddard Earth Sciences Data and Information Services Center (GES
 415 DISC), [Date Accessed: 24 May 2017]. 10.5067/GPM/GMI/GPM/1B/05
 416 GPM Science Team, 2017a: GPM TMI on TRMM Common Calibrated Brightness Temperatures
 417 L1C 1.5 hours 13 km V05, Greenbelt, MD, USA, Goddard Earth Sciences Data and
 418 Information Services Center (GES DISC), [Date Accessed: 28 Dec
 419 2017]. 10.5067/GPM/TMI/TRMM/1C/05
 420 GPM Science Team, 2017b: GPM AMSR-E on AQUA Common Calibrated Brightness
 421 Temperatures L1C 1.5 hours 10.5 km V05, Greenbelt, MD, USA, Goddard Earth Sciences
 422 Data and Information Services Center (GES DISC), [Date Accessed: 28 Dec
 423 2017]. 10.5067/GPM/AMSRE/AQUA/1C/05
 424 GPM Science Team, 2017c: GPM SSMI on F14 Common Calibrated Brightness Temperatures
 425 L1C 1.5 hours 13 km V05, Greenbelt, MD, USA, Goddard Earth Sciences Data and
 426 Information Services Center (GES DISC), [Date Accessed: 28 Dec
 427 2017]. 10.5067/GPM/SSMI/F14/1C/05
 428 Grody, N.C., 1984: Precipitation monitoring over land from satellites by microwave radiometry.
 429 *Proc. IGARSS'84 Sympos.*, Strasbourg, 27-30 Aug 1984.
 430 Hollinger, J.P., J.L. Pierce, and G.A. Poe, 1990: SSM/I instrument evaluation. *IEEE Trans. Geosci.*
 431 *Rem. Sens.*, **28**, 781-790.
 432 Hou, A.Y., R.K. Kakar, S. Neeck, A.A. Azarbarzin, C.D. Kummerow, M. Kojima, R. Oki, K.
 433 Nakamura, T. Iguchi, 2014: The Global Precipitation Measurement Mission. *Bull. Amer.*
 434 *Meteor., Soc.*, **95**, 701-722.

- Iguchi, T. and R. Meneghini, 2016: GPM GMI (GPROF) Radiometer Precipitation Profiling L2A 1.5 hours 13 km V05, Greenbelt, MD, Goddard Earth Sciences Data and Information Services Center (GES DISC), [Date Accessed: 24 May 2017]. 10.5067/GPM/GMI/GPM/GPROF/2A/05
- JAXA, 2006: AMSR-E data users handbook. 4th Ed. *Japan Aerospace Exploration Agency*. Available from http://www.eorc.jaxa.jp/en/hatoyama/amsr-e/amsr-e_handbook_e.pdf.
- Jiang, H., J.P. Zagrodnik, C. Tao, and E.J. Zipser, 2018: Classifying precipitation types in tropical cyclones using the NRL 37 GHz color product. *J. Geophys. Res. – Atmos., early online release*, <https://doi.org/10.1029/2018JD028324>.
- Kidd, C., 1998: On rainfall retrieval using polarization-corrected temperatures. *Int. J. Remote Sensing*, **19**, 981-996.
- Kummerow, C., W. Barnes, T. Kozu, J. Shiue, J. Simpson, 1998: The Tropical Rainfall Measuring Mission (TRMM) sensor package. *J. Atmos. Ocean. Tech.*, **15**, 809-817.
- Lee, T.F., F.J. Turk, J. Hawkins, and K. Richardson, 2002: Interpretation of TRMM TMI images of tropical cyclones. *Earth Interactions*, **6**, 1-17.
- Liu, C., E.J. Zipser, D.J. Cecil, S.W. Nesbitt, and S. Sherwood, 2008: A cloud and precipitation feature database from nine years of TRMM observations. *J. Appl. Meteor. Clim.*, **47**, 2712-2728.
- Mohr, K.I. and E.J. Zipser, 1996: Defining mesoscale convective systems by their 85-GHz ice-scattering signatures. *Bull. Amer. Meteor. Soc.*, **77**, 1179-1189.
- Mroz, K., A. Battaglia, T.J. Lang, D.J. Cecil, S. Tanelli, and F. Tridon, 2017: Hail detection algorithm for the GPM core satellite sensors. *J. Appl. Meteor. Clim.*, **56**, 1939-1957. <https://doi.org/10.1175/JAMC-D-16-0368.1>.

458 Nesbitt, S.W., E.J. Zipser, and D.J. Cecil, 2000: A census of precipitation features in the tropics
 459 using TRMM: Radar, ice scattering, and lightning observations. *J. Climate*, **13**, 4087-4106.
 460 Price, C.G., and B.P. Murphy, 2002: Lightning activity during the 1999 Superior derecho.
 461 *Geophys. Res. Lett.*, **29**, 57-1 -57-4.
 462 Spencer, R.W., H.M. Goodman, and R.E. Hood, 1989: Precipitation retrieval over land and ocean
 463 with the SSM/I: Identification and characteristics of the scattering signal. *J. Atmos.*
 464 *Oceanic Technol.*, **6**, 254-273.
 465 Todd, M.C. and J.O. Bailey, 1995: Estimates of rainfall over the United Kingdom and surrounding
 466 seas from the SSM/I using the polarization-corrected temperature algorithm. *J. Appl.*
 467 *Meteor.*, **34**, 1254-1265.
 468 Toracinta, E.R., D.J. Cecil, E.J. Zipser, S.W. Nesbitt, 2002: Radar, passive microwave, and
 469 lightning characteristics of precipitating systems in the tropics. *Mon. Wea. Rev.*, **130**, 802-
 470 824.
 471 Tropical Rainfall Measuring Mission (TRMM), 2017: GPM TMI on TRMM Brightness
 472 Temperatures L1B 1.5 hours 13 km V05, Greenbelt, MD, Goddard Earth Sciences Data
 473 and Information Services Center (GES DISC), [Date Accessed: 28 Dec 2017].
 474 10.5067/GPM/TMI/TRMM/1B/05
 475 Weinman, J.A. and P.J. Guetter, 1977: Determination of rainfall distributions from microwave
 476 radiation measured by Nimbus 6 ESMR. *J. Appl. Meteor.*, **16**, 437-442.
 477 Yang, S., J. Hawkins, and K. Richardson, 2014: The improved NRL tropical cyclone monitoring
 478 system wit a unified microwave brightness temperature calibration scheme. *Remote Sens.*,
 479 **6**, 4563-4581.

480 Zipser, E.J., C. Liu, D.J. Cecil, S.W. Nesbitt, and D.P. Yorty, 2006: Where are the most intense
481 thunderstorms on Earth? *Bull. Amer. Meteor. Soc.*, **87**, 1057-1071.
482

8. Tables

Table 1. Sample size (in millions) of land-ocean pairings for each 5° latitude bin (bottom latitude of the bin is listed in the first column) and each month.

Lat	Jan	Feb	Mar	Apr	May	Jun	Jul	Aug	Sep	Oct	Nov	Dec
55	2	4	17	136	273	293	338	357	308	200	38	6
50	6	8	26	153	209	225	241	255	221	164	53	11
45	12	21	65	133	159	173	180	193	165	143	85	29
40	43	47	91	112	118	119	127	133	120	115	96	62
35	81	75	112	122	128	129	125	128	116	117	109	96
30	72	68	86	87	89	84	82	86	80	79	87	87
25	78	70	82	75	69	61	52	53	60	60	74	84
20	75	71	86	76	73	65	40	34	38	45	60	73
15	58	59	73	68	58	45	36	37	38	32	45	55
10	108	111	120	101	92	85	72	77	86	82	89	100
5	104	112	123	95	96	94	91	95	91	89	98	100
0	103	97	101	86	98	97	98	108	108	102	100	100
-5	86	80	80	72	92	91	95	103	100	95	91	88
-10	85	80	84	83	103	102	110	121	119	111	103	89
-15	89	83	90	94	120	113	121	132	130	124	108	94
-20	81	78	85	86	104	95	99	108	114	104	99	86
-25	77	75	79	79	95	84	87	92	93	82	82	77
-30	76	72	74	78	95	83	85	90	91	81	83	76
-35	90	88	83	86	97	88	89	93	97	88	95	91
-40	50	48	47	45	46	42	41	41	44	41	48	52
-45	28	27	26	26	25	22	20	20	22	23	26	28
-50	17	16	16	16	17	13	12	12	16	15	16	18
-55	6	5	6	6	6	5	3	3	5	5	5	6

Table 2. Footprint sizes (effective fields of view, in km) for the frequencies and instruments used in this study.

Sensor	GMI (Hou et al. 2014)				TMI (Kummerow et al. 1998)				AMSR-E (JAXA 2006)				SSM/I (Hollinger et al. 1990)		
Frequency (GHz)	10.65	18.7	36.5	89.0	10.7	19.35	37.0	85.5	10.65	18.7	36.5	89.0	19.35	37.0	85.5
Along-track	32	18	15	7	63	30	16	7	51	27	14	6	69	37	15
Cross-track	19	11	9	4	37	18	9	5	29	16	8	4	43	28	13

494 Table 3. 89-GHz PCT coefficient Θ_{89} for each latitude and month that gives the most land-ocean
 495 pixel pairs with PCT differences < 2 K.

496

Lat	Jan	Feb	Mar	Apr	May	Jun	Jul	Aug	Sep	Oct	Nov	Dec
55	0.54	0.57	0.60	0.63	0.64	0.72	0.74	0.69	0.61	0.55	0.58	0.62
50	0.52	0.53	0.56	0.60	0.64	0.80	0.74	0.72	0.63	0.55	0.56	0.57
45	0.55	0.58	0.60	0.66	0.69	0.79	0.77	0.67	0.64	0.58	0.57	0.58
40	0.51	0.56	0.58	0.59	0.64	0.72	0.66	0.63	0.61	0.58	0.55	0.53
35	0.48	0.55	0.55	0.63	0.65	0.75	0.67	0.66	0.62	0.57	0.51	0.48
30	0.46	0.51	0.58	0.65	0.69	0.78	0.70	0.65	0.66	0.56	0.49	0.41
25	0.44	0.56	0.65	0.73	0.82	0.70	0.68	0.66	0.61	0.59	0.55	0.46
20	0.51	0.57	0.70	0.83	0.81	0.74	0.64	0.51	0.54	0.58	0.56	0.51
15	0.59	0.64	0.68	0.77	0.73	0.68	0.64	0.59	0.57	0.54	0.58	0.58
10	0.62	0.68	0.73	0.85	0.87	0.85	0.74	0.64	0.66	0.69	0.60	0.61
5	0.65	0.71	0.73	0.69	0.66	0.63	0.57	0.53	0.58	0.61	0.62	0.61
0	0.58	0.63	0.57	0.52	0.52	0.56	0.59	0.57	0.59	0.60	0.60	0.60
-5	0.59	0.62	0.56	0.52	0.56	0.61	0.61	0.64	0.64	0.63	0.61	0.61
-10	0.52	0.55	0.49	0.51	0.57	0.65	0.66	0.68	0.70	0.67	0.57	0.53
-15	0.53	0.50	0.50	0.52	0.59	0.65	0.65	0.68	0.69	0.64	0.58	0.51
-20	0.68	0.62	0.59	0.63	0.61	0.64	0.62	0.64	0.72	0.75	0.72	0.68
-25	0.81	0.77	0.70	0.67	0.66	0.61	0.60	0.63	0.73	0.81	0.78	0.82
-30	0.84	0.85	0.77	0.72	0.63	0.59	0.60	0.63	0.70	0.81	0.77	0.84
-35	0.84	0.80	0.74	0.68	0.64	0.57	0.60	0.61	0.65	0.75	0.73	0.79
-40	0.78	0.76	0.72	0.63	0.62	0.58	0.58	0.58	0.62	0.72	0.72	0.77
-45	0.71	0.66	0.62	0.58	0.55	0.49	0.52	0.54	0.55	0.66	0.62	0.67
-50	0.74	0.67	0.67	0.61	0.56	0.51	0.53	0.56	0.56	0.62	0.69	0.70
-55	0.81	0.69	0.70	0.59	0.57	0.57	0.56	0.58	0.61	0.59	0.76	0.71

497

Table 4. 37-GHz PCT coefficient Θ_{37} for each latitude and month that gives the most land-ocean pixel pairs with PCT differences < 2 K.

Lat	Jan	Feb	Mar	Apr	May	Jun	Jul	Aug	Sep	Oct	Nov	Dec
55	0.97	0.98	1.01	1.03	1.03	1.11	1.12	1.10	1.05	0.98	0.98	1.00
50	0.96	0.97	0.99	1.03	1.07	1.17	1.13	1.13	1.08	1.02	1.00	0.98
45	0.98	1.01	1.03	1.07	1.11	1.17	1.18	1.14	1.11	1.04	1.02	1.00
40	0.97	1.01	1.01	1.03	1.09	1.15	1.12	1.12	1.09	1.05	1.01	0.99
35	0.95	1.01	1.04	1.08	1.12	1.18	1.17	1.14	1.12	1.07	1.01	0.98
30	0.96	0.99	1.07	1.11	1.14	1.20	1.17	1.14	1.13	1.08	1.01	0.98
25	0.97	1.06	1.07	1.14	1.13	1.12	1.12	1.10	1.10	1.06	1.05	0.99
20	1.02	1.09	1.13	1.20	1.14	1.14	1.11	1.05	1.06	1.06	1.05	1.04
15	1.08	1.12	1.15	1.19	1.16	1.14	1.17	1.10	1.09	1.06	1.07	1.07
10	1.25	1.27	1.35	1.42	1.32	1.28	1.24	1.17	1.16	1.16	1.17	1.23
5	1.14	1.19	1.18	1.15	1.13	1.12	1.08	1.07	1.07	1.08	1.08	1.11
0	1.07	1.10	1.08	1.05	1.04	1.06	1.06	1.06	1.07	1.07	1.06	1.06
-5	1.08	1.10	1.07	1.05	1.07	1.09	1.09	1.10	1.11	1.09	1.10	1.07
-10	1.08	1.09	1.06	1.06	1.09	1.12	1.12	1.16	1.15	1.14	1.09	1.08
-15	1.08	1.08	1.06	1.05	1.09	1.11	1.12	1.14	1.15	1.13	1.10	1.07
-20	1.16	1.15	1.12	1.12	1.11	1.14	1.13	1.17	1.23	1.30	1.26	1.18
-25	1.25	1.24	1.21	1.17	1.17	1.17	1.16	1.21	1.25	1.35	1.30	1.30
-30	1.27	1.23	1.21	1.19	1.16	1.13	1.12	1.16	1.21	1.28	1.23	1.30
-35	1.31	1.22	1.23	1.19	1.14	1.08	1.09	1.13	1.15	1.20	1.21	1.27
-40	1.22	1.18	1.18	1.11	1.10	1.04	1.04	1.06	1.07	1.15	1.17	1.21
-45	1.20	1.19	1.14	1.08	1.08	1.01	1.01	1.04	1.04	1.12	1.14	1.18
-50	1.30	1.22	1.21	1.09	1.09	1.04	1.05	1.08	1.08	1.14	1.22	1.22
-55	1.27	1.17	1.17	1.08	1.05	1.04	1.04	1.05	1.07	1.08	1.17	1.17

Table 5. 19-GHz PCT coefficient Θ_{19} for each latitude and month that gives the most land-ocean pixel pairs with PCT differences < 2 K.

Lat	Jan	Feb	Mar	Apr	May	Jun	Jul	Aug	Sep	Oct	Nov	Dec
55	1.29	1.30	1.32	1.33	1.34	1.43	1.42	1.40	1.34	1.28	1.29	1.29
50	1.28	1.29	1.34	1.37	1.39	1.49	1.44	1.42	1.38	1.33	1.32	1.29
45	1.28	1.35	1.40	1.43	1.44	1.48	1.49	1.44	1.41	1.37	1.35	1.31
40	1.29	1.34	1.34	1.36	1.40	1.45	1.43	1.40	1.38	1.35	1.32	1.29
35	1.28	1.34	1.36	1.40	1.43	1.48	1.48	1.43	1.40	1.37	1.31	1.28
30	1.23	1.28	1.36	1.41	1.42	1.47	1.42	1.38	1.38	1.33	1.26	1.25
25	1.24	1.29	1.33	1.39	1.39	1.38	1.37	1.35	1.34	1.31	1.30	1.26
20	1.29	1.37	1.37	1.42	1.39	1.38	1.35	1.29	1.31	1.31	1.30	1.31
15	1.32	1.38	1.42	1.41	1.38	1.37	1.38	1.33	1.33	1.30	1.31	1.31
10	1.62	1.69	1.74	1.79	1.57	1.52	1.48	1.42	1.41	1.39	1.39	1.39
5	1.37	1.43	1.41	1.38	1.37	1.36	1.33	1.31	1.32	1.32	1.33	1.35
0	1.32	1.34	1.32	1.30	1.29	1.31	1.30	1.31	1.32	1.31	1.31	1.31
-5	1.33	1.35	1.32	1.30	1.32	1.33	1.33	1.34	1.35	1.34	1.34	1.32
-10	1.32	1.33	1.31	1.30	1.33	1.35	1.36	1.39	1.39	1.37	1.34	1.32
-15	1.33	1.33	1.31	1.30	1.33	1.35	1.37	1.40	1.41	1.39	1.35	1.32
-20	1.42	1.39	1.38	1.37	1.35	1.41	1.43	1.46	1.59	1.63	1.58	1.46
-25	1.53	1.48	1.48	1.44	1.46	1.49	1.51	1.56	1.59	1.70	1.68	1.59
-30	1.49	1.47	1.44	1.42	1.40	1.40	1.43	1.42	1.47	1.59	1.48	1.51
-35	1.57	1.47	1.49	1.46	1.42	1.39	1.41	1.43	1.44	1.51	1.49	1.58
-40	1.48	1.44	1.44	1.39	1.40	1.34	1.35	1.38	1.38	1.45	1.47	1.49
-45	1.67	1.66	1.59	1.38	1.49	1.39	1.39	1.45	1.41	1.49	1.56	1.68
-50	1.79	1.75	1.72	1.55	1.53	1.49	1.51	1.53	1.53	1.61	1.73	1.75
-55	1.66	1.59	1.57	1.47	1.43	1.43	1.44	1.45	1.43	1.48	1.55	1.59

Table 6. 10-GHz PCT coefficient Θ_{10} for each latitude and month that gives the most land-ocean pixel pairs with PCT differences < 2 K.

Lat	Jan	Feb	Mar	Apr	May	Jun	Jul	Aug	Sep	Oct	Nov	Dec
55	1.47	1.50	1.53	1.53	1.53	1.61	1.58	1.55	1.49	1.45	1.47	1.48
50	1.47	1.50	1.55	1.54	1.54	1.65	1.58	1.55	1.52	1.49	1.48	1.47
45	1.44	1.49	1.73	1.79	1.58	1.63	1.63	1.57	1.55	1.53	1.49	1.47
40	1.48	1.54	1.56	1.57	1.58	1.62	1.58	1.53	1.52	1.51	1.49	1.48
35	1.45	1.53	1.57	1.60	1.61	1.63	1.62	1.51	1.50	1.52	1.46	1.46
30	1.36	1.40	1.50	1.55	1.55	1.57	1.52	1.48	1.48	1.44	1.38	1.37
25	1.36	1.41	1.46	1.49	1.50	1.50	1.47	1.45	1.44	1.42	1.38	1.37
20	1.40	1.47	1.47	1.51	1.50	1.47	1.45	1.40	1.42	1.42	1.42	1.43
15	1.42	1.47	1.50	1.49	1.48	1.47	1.46	1.43	1.43	1.41	1.41	1.42
10	1.79	1.79	1.79	1.78	1.68	1.64	1.58	1.53	1.51	1.48	1.48	1.79
5	1.46	1.50	1.49	1.46	1.46	1.45	1.43	1.42	1.43	1.42	1.43	1.43
0	1.42	1.44	1.43	1.42	1.41	1.42	1.40	1.41	1.42	1.42	1.42	1.41
-5	1.43	1.45	1.42	1.41	1.42	1.43	1.43	1.44	1.45	1.44	1.45	1.43
-10	1.43	1.44	1.42	1.40	1.43	1.45	1.45	1.49	1.49	1.47	1.44	1.43
-15	1.44	1.44	1.42	1.41	1.43	1.45	1.50	1.51	1.52	1.49	1.46	1.43
-20	1.54	1.50	1.49	1.47	1.45	1.57	1.59	1.66	1.75	1.79	1.79	1.61
-25	1.64	1.57	1.61	1.55	1.67	1.71	1.73	1.78	1.79	1.79	1.79	1.79
-30	1.59	1.56	1.54	1.53	1.51	1.51	1.58	1.56	1.60	1.73	1.61	1.62
-35	1.69	1.58	1.62	1.58	1.58	1.55	1.57	1.59	1.61	1.71	1.66	1.72
-40	1.62	1.57	1.55	1.52	1.55	1.50	1.52	1.59	1.54	1.59	1.61	1.61
-45	1.56	1.53	1.53	1.79	1.79	1.76	1.77	1.79	1.79	1.79	1.53	1.53
-50	1.62	1.56	1.59	1.79	1.79	1.79	1.79	1.79	1.79	1.79	1.58	1.59
-55	1.79	1.79	1.79	1.79	1.79	1.77	1.79	1.78	1.76	1.79	1.79	1.79

Table 7. PCT coefficients Θ from this study, and from the literature.

source	85-89 GHz	36-37 GHz	19 GHz	10 GHz
This study	0.70 (GMI)	1.15 (GMI)	1.40 (GMI)	1.50 (GMI)
Spencer et al. 1989	0.818 (SSMI) 0.54-0.61 (model)			
Toracinta et al. 2002		1.20 (TMI)		
Weinman and Guetter 1977		1.50 (ESMR) 1.20 (model)		
Grody (1984)		1.08 (SMMR)	1.38 (SMMR)	
Barrett and Kidd (1990)	0.64 (SSMI)			
Todd and Bailey (1995); Kidd (1998)	0.5-0.75 (SSMI)			
Lee et al. (2002)		1.18		

9. List of Figures

Figure 1. Example convective outbreak in Texas, 2225 UTC 26 May 2015. (a) Ground-based radar reflectivity mosaic. (b-d) GMI 37-GHz, 19-GHz, and 10-GHz vertically polarized brightness temperatures. Contour interval in (b-d) is 25 K, with thick contours every 50 K and the minimum brightness temperature in the domain printed in the panel title.

Figure 2. Percentage of land-ocean PCT differences less than 2 K (thick lines) and less than 10 K (thin lines), as a function of Θ value.

Figure 3. Probability density functions of the land-ocean PCT difference (bin size = 2 K) for selected PCT coefficients Θ .

Figure 4. Two-dimensional probability density functions of the land-ocean PCT difference (bin size = 2 K) for Θ coefficients ranging from 0.30 to 1.79 (increments of 0.01). Contour interval 1%, with thick lines at 5% intervals.

Figure 5. Percentage of land-ocean PCT differences less than 2 K (thick lines) and less than 10 K (thin lines), as a function of Θ value, for the 0° - 5° N latitude bin in July.

Figure 6. Percentage of land-ocean PCT differences less than 2 K (thick lines) and less than 10 K (thin lines), as a function of Θ value, for the 35° - 40° N latitude bin in July.

Figure 7. Difference between PCT_{89} computed using $\Theta_{85}=0.818$ (Spencer et al. 1989) minus that using $\Theta_{89}=0.70$ (from this study). Three days of GPM orbits (26-28 May 2015) are mapped.

Figure 8. Difference between PCT_{37} computed using $\Theta_{37}=1.20$ (Toracinta et al. 2002) minus that using $\Theta_{37}=1.15$ (from this study). Three days of GPM orbits (26-28 May 2015) are mapped.

Figure 9. GMI case from west of Fort Worth, Texas, 26 May 2015. Left panels are vertically polarized brightness temperature, right columns are PCT. Contour interval 25 K, with thick contours every 50 K. The minimum brightness temperature (or PCT) in the domain is printed.

Figure 10. As in Fig. 9, for TMI case from northern Argentina, 30 Dec 1997. In (a-b), TB_{85V} and PCT_{85} were re-derived with XCAL offsets applied to level 1B files, because the level 1C XCAL files have values below 50 K set as missing.

Figure 11. As in Fig. 9, for AMSR-E case Typhoon Bolaven east of the Philippines, 18 Nov 2005. In (a-b), TB_{89V} and PCT_{89} were taken from AMSR-E Level 2A brightness temperatures distributed by NSIDC, because the level 1C XCAL files have values below 50 K set as missing. Comparison of nearby pixels slightly above 50 K suggests the calibrations are consistent within 1.0 K.

Figure 12. SSMI case from Minnesota, 04 July 1999. Left panels are vertically polarized brightness temperature, right columns are PCT. Contour interval 25 K, with thick contours every 50 K. The minimum brightness temperature (or PCT) in the domain is printed.

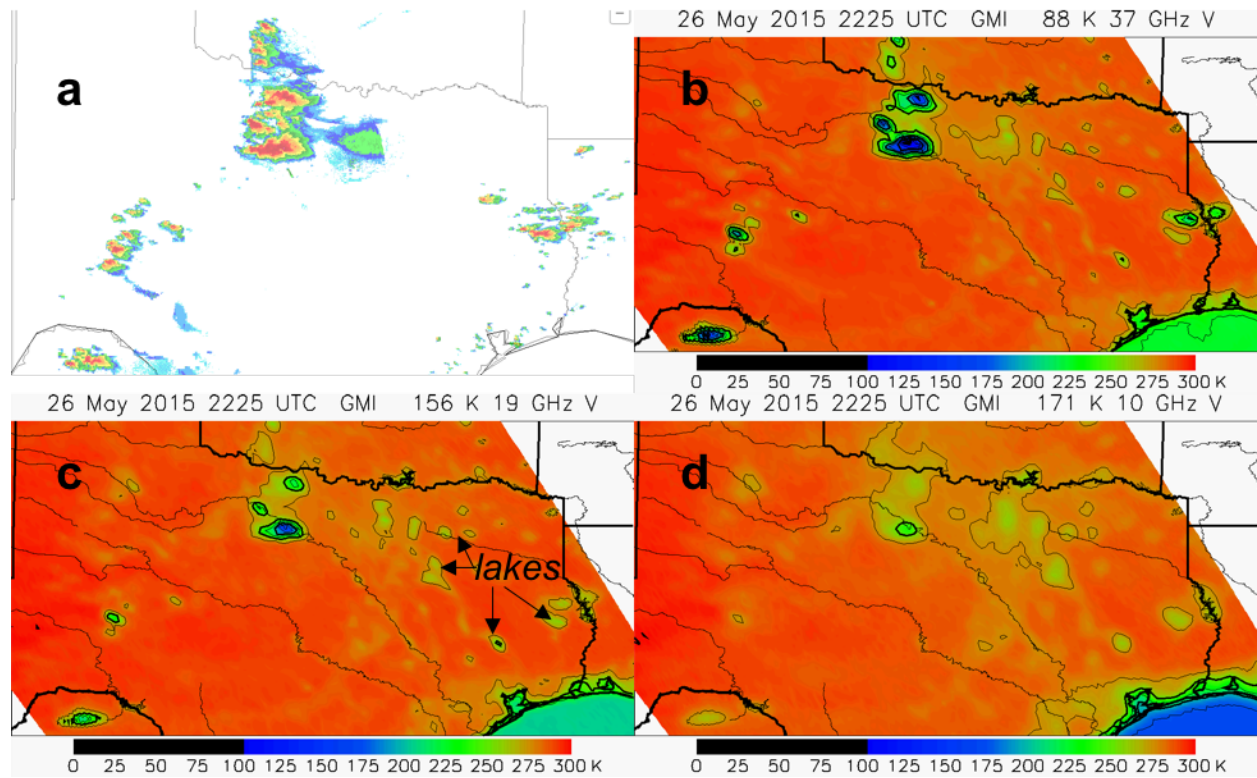


Figure 1. Example convective outbreak in Texas, 2225 UTC 26 May 2015. (a) Ground-based radar reflectivity mosaic. (b-d) GMI 37-GHz, 19-GHz, and 10-GHz vertically polarized brightness temperatures. Contour interval in (b-d) is 25 K, with thick contours every 50 K and the minimum brightness temperature in the domain printed in the panel title.

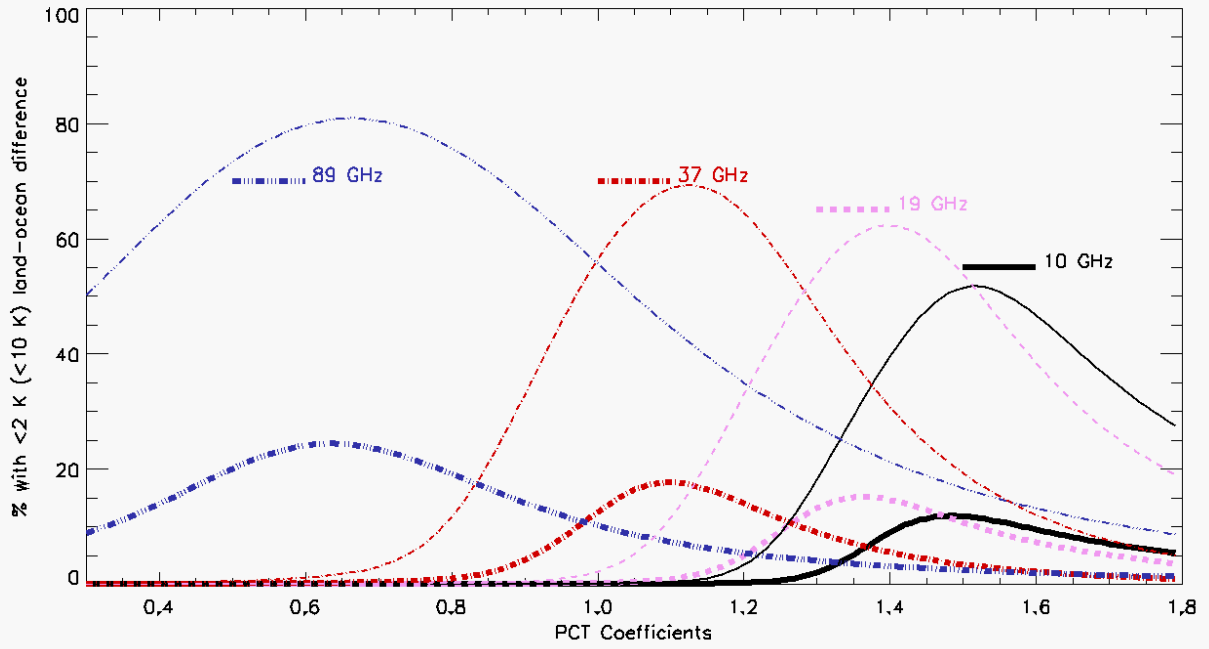


Figure 2. Percentage of land-ocean PCT differences less than 2 K (thick lines) and less than 10 K (thin lines), as a function of Θ value.

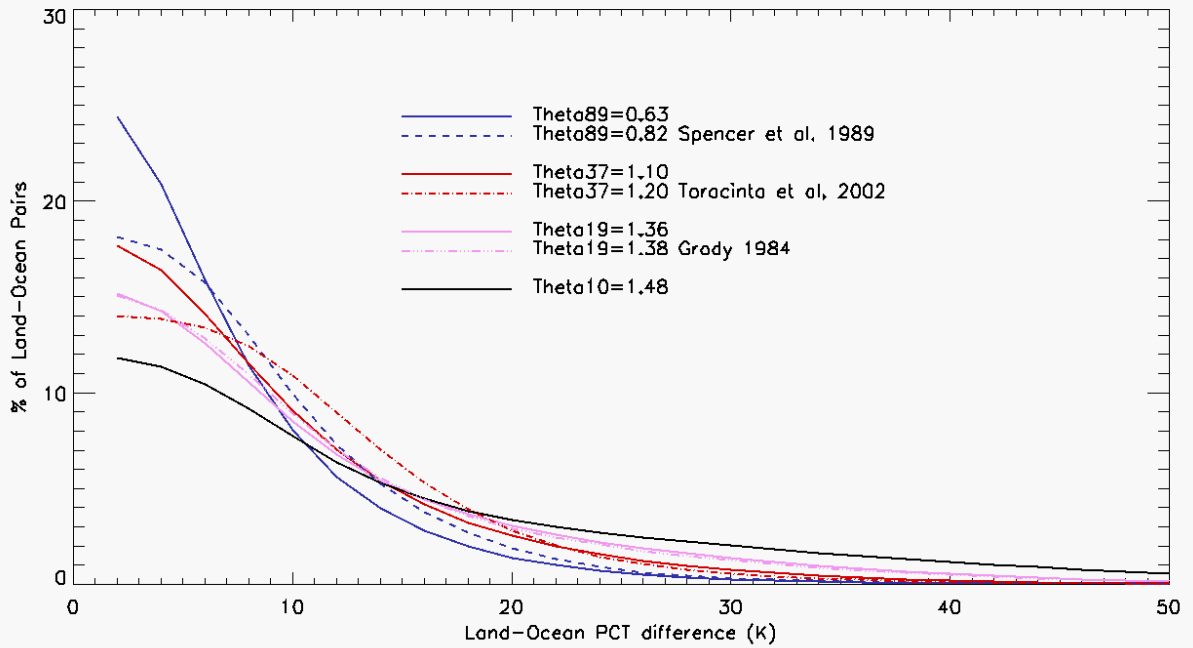


Figure 3. Probability density functions of the land-ocean PCT difference (bin size = 2 K) for selected PCT coefficients Θ .

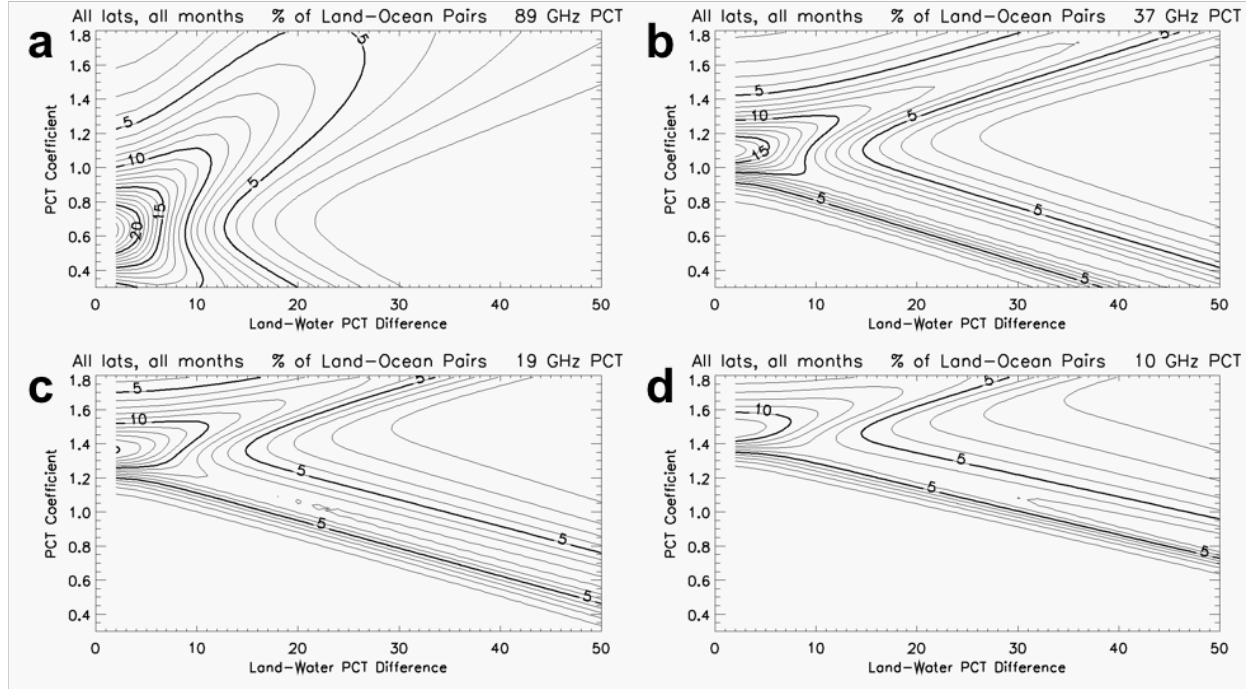


Figure 4. Two-dimensional probability density functions of the land-ocean PCT difference (bin size = 2 K) for Θ coefficients ranging from 0.30 to 1.79 (increments of 0.01). Contour interval 1%, with thick lines at 5% intervals.

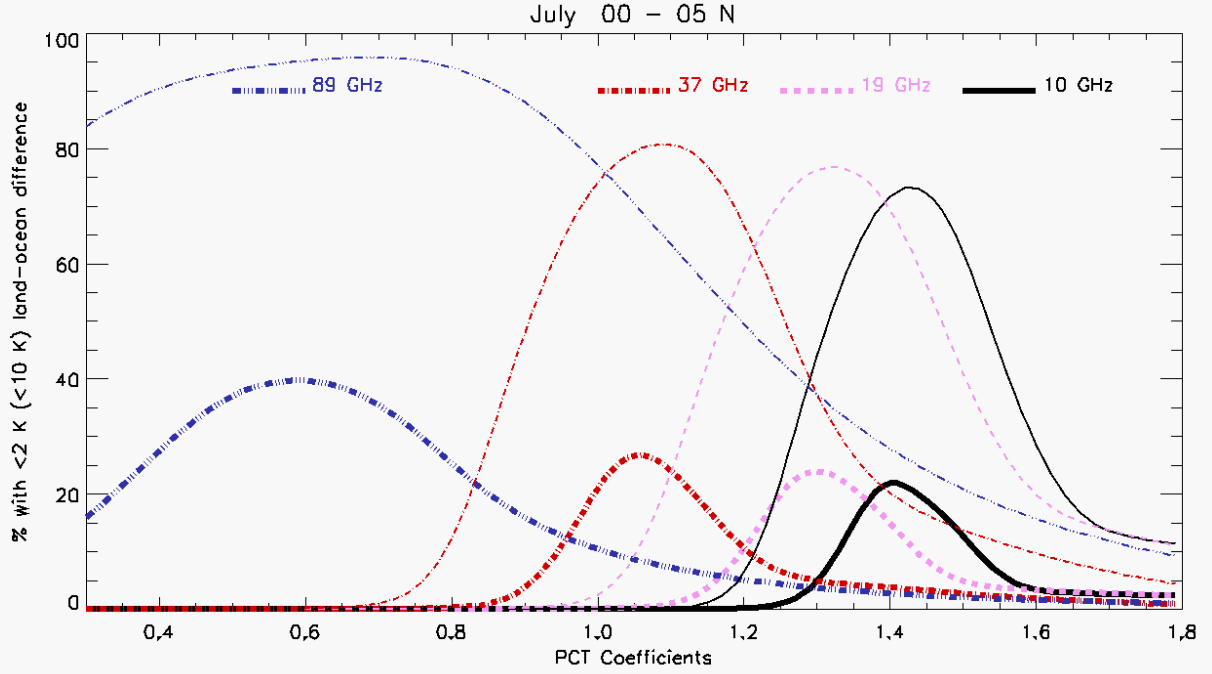


Figure 5. Percentage of land-ocean PCT differences less than 2 K (thick lines) and less than 10 K (thin lines), as a function of Θ value, for the 0° - 5° N latitude bin in July.

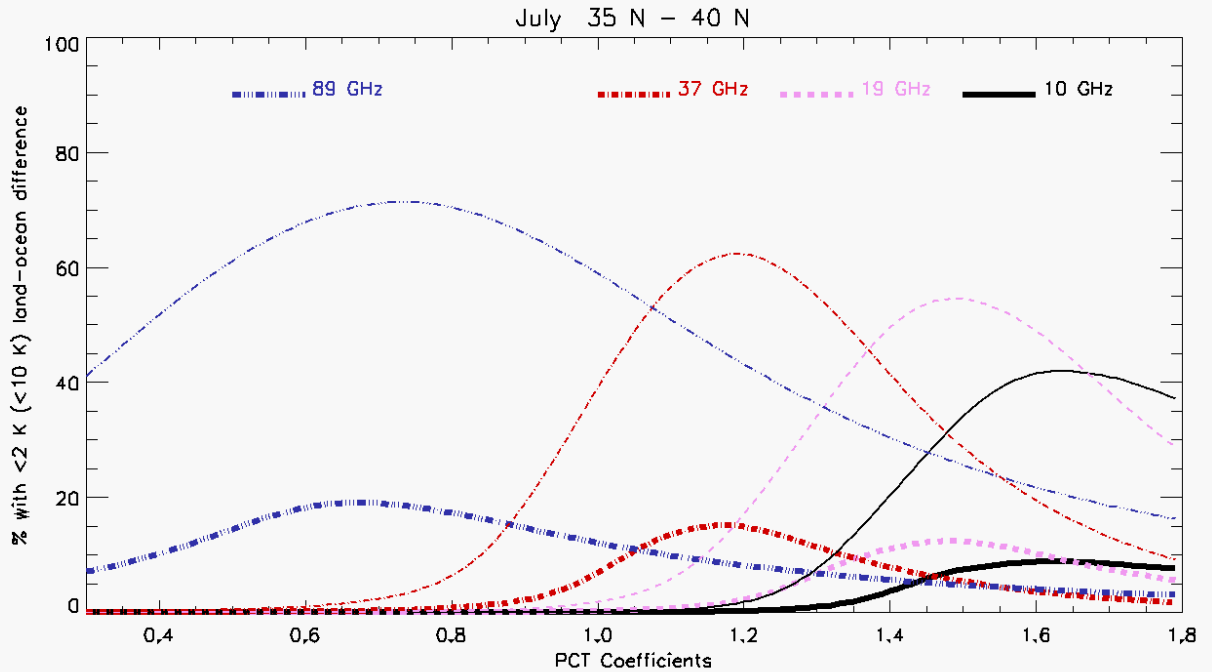


Figure 6. Percentage of land-ocean PCT differences less than 2 K (thick lines) and less than 10 K (thin lines), as a function of Θ value, for the 35° - 40° N latitude bin in July.

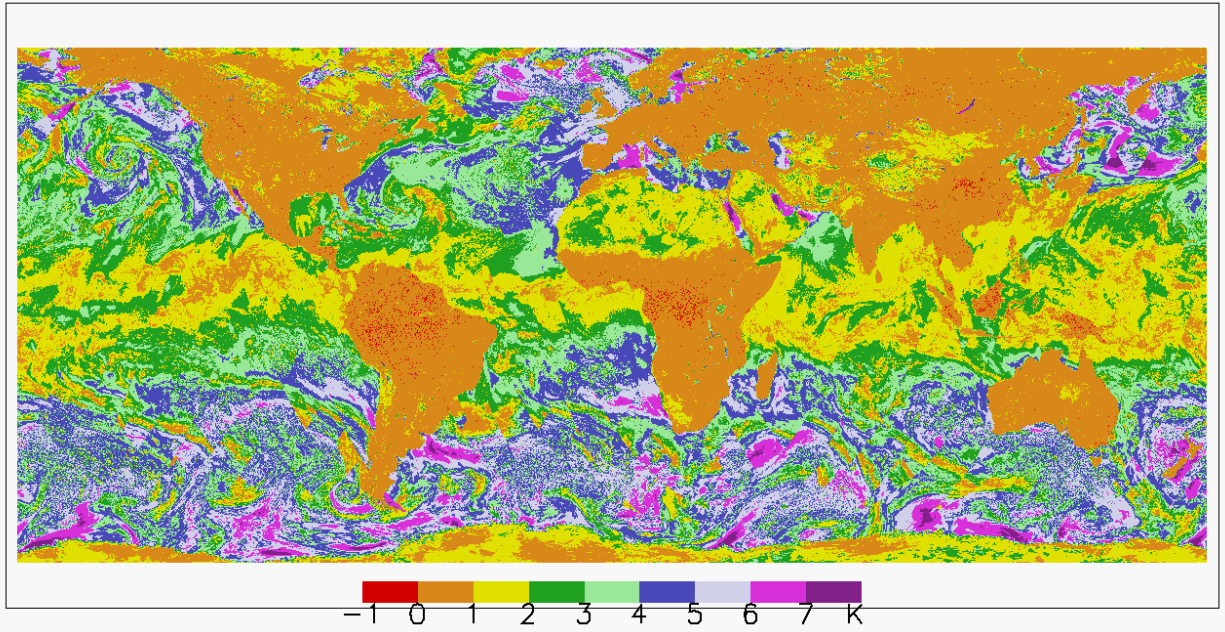


Figure 7. Difference between PCT_{89} computed using $\Theta_{85}=0.818$ (Spencer et al. 1989) minus that using $\Theta_{89}=0.70$ (from this study). Three days of GPM orbits (26-28 May 2015) are mapped.

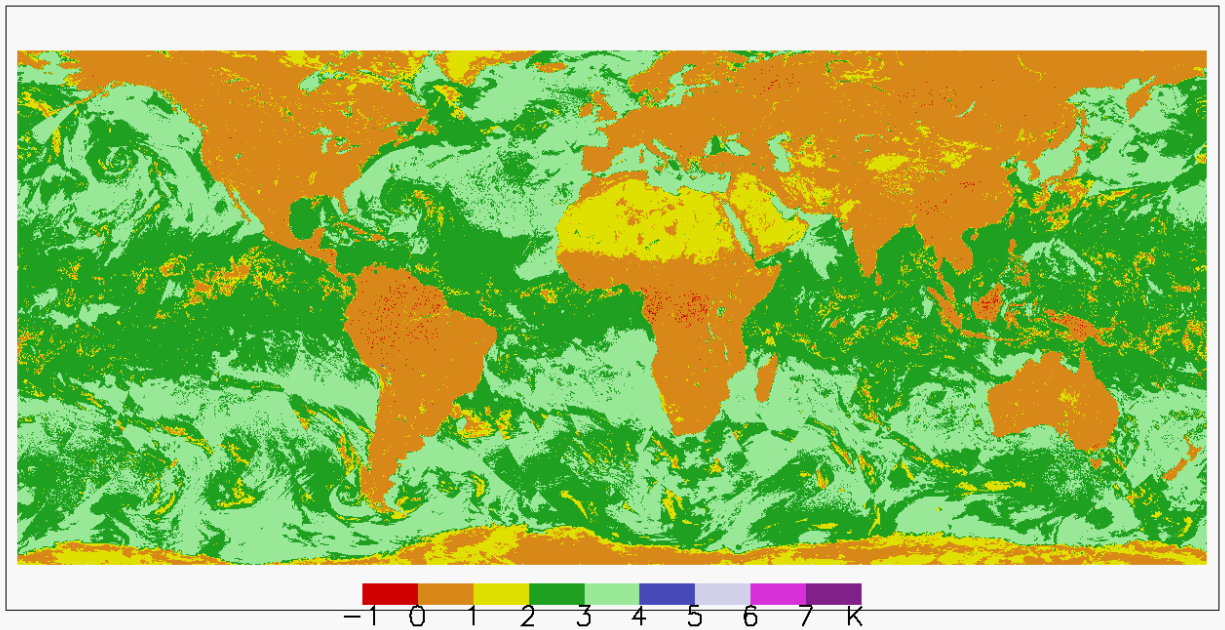


Figure 8. Difference between PCT_{37} computed using $\Theta_{37}=1.20$ (Toracinta et al. 2002) minus that using $\Theta_{37}=1.15$ (from this study). Three days of GPM orbits (26-28 May 2015) are mapped.

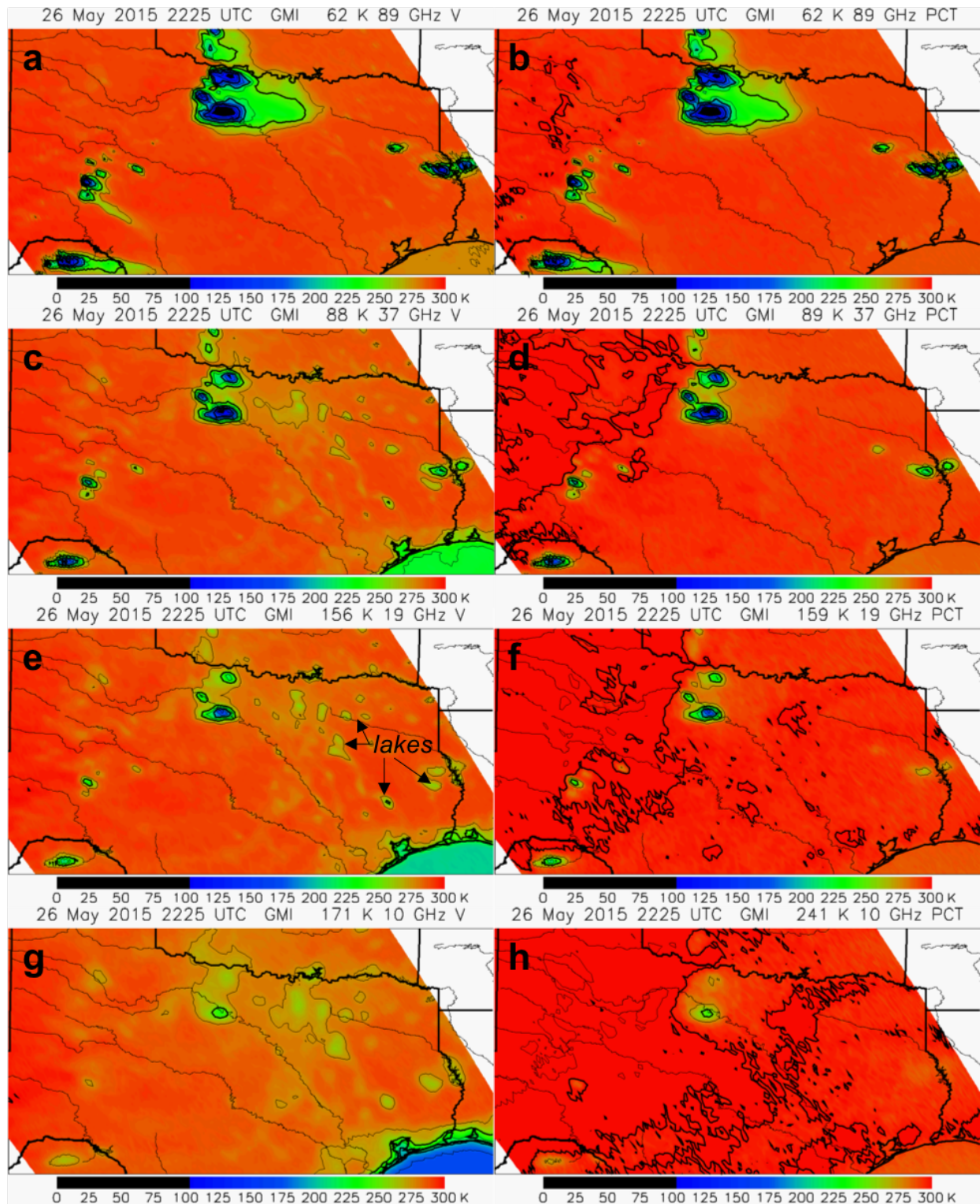


Figure 9. GMI case from west of Fort Worth, Texas, 26 May 2015. Left panels are vertically polarized brightness temperature, right columns are PCT. Contour interval 25 K, with thick contours every 50 K. The minimum brightness temperature (or PCT) in the domain is printed.

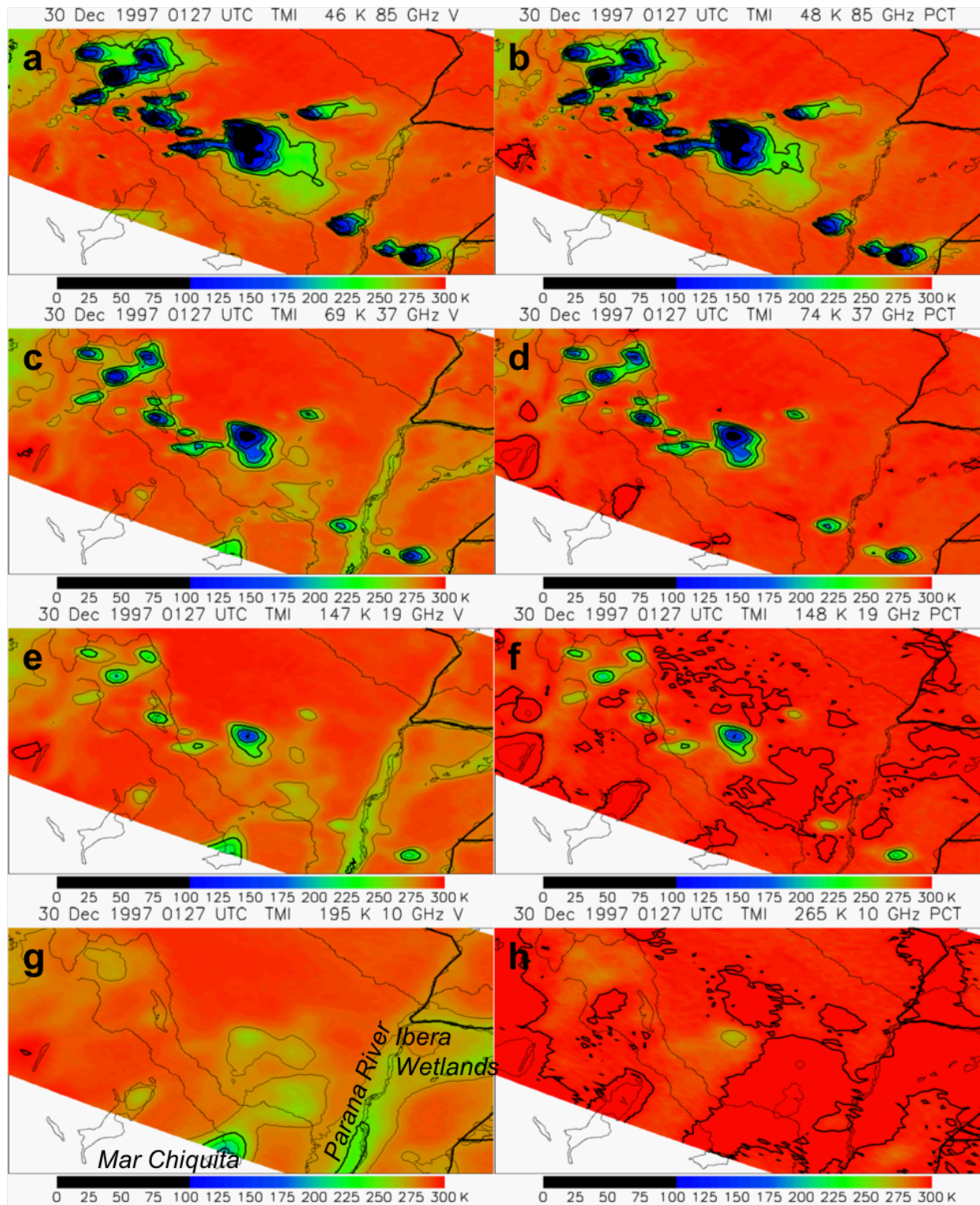


Figure 10. As in Fig. 9, for TMI case from northern Argentina, 30 Dec 1997. In (a-b), TB_{85V} and PCT_{85} were re-derived with XCAL offsets applied to level 1B files, because the level 1C XCAL files have values below 50 K set as missing.

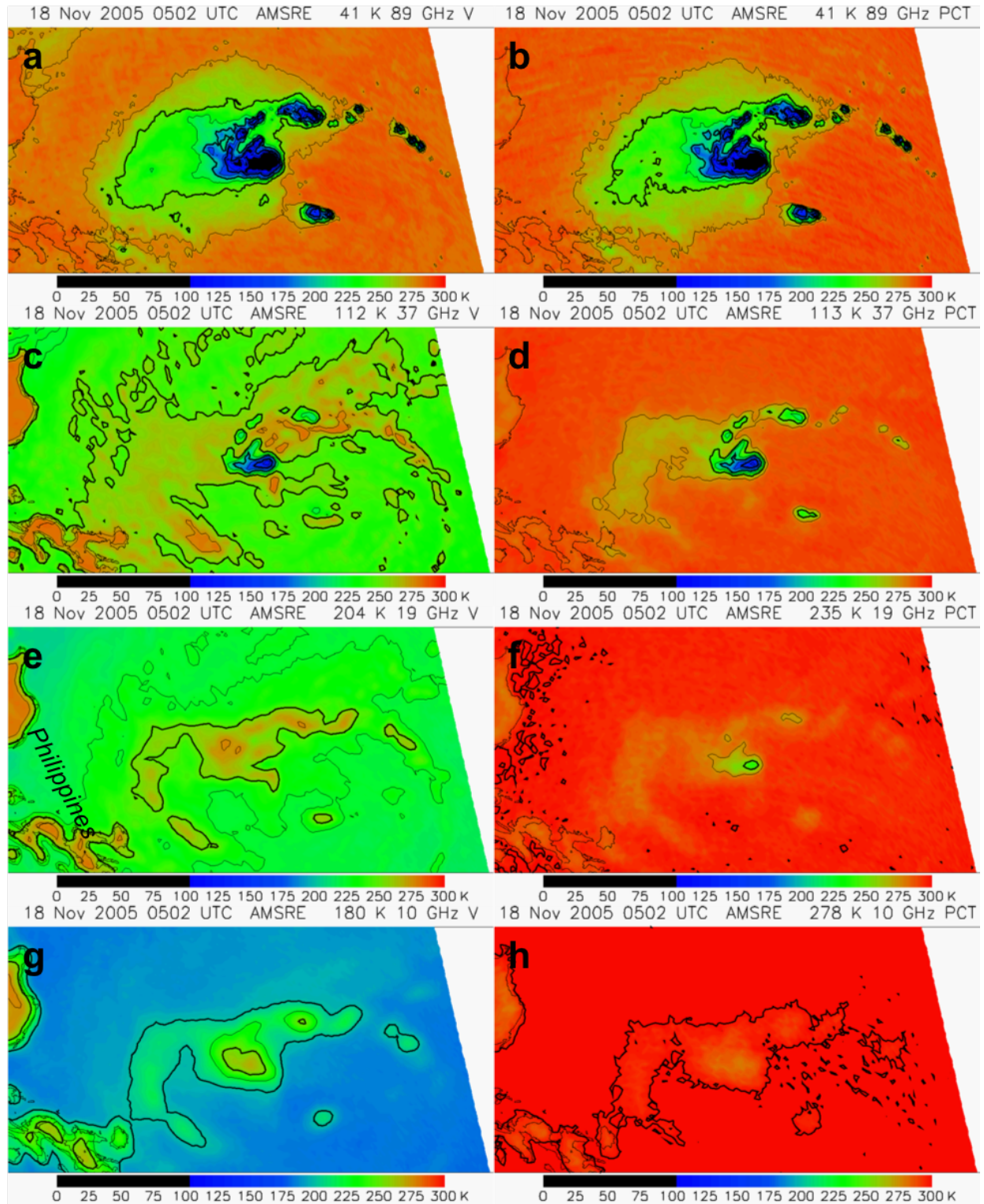


Figure 11. As in Fig. 9, for AMSR-E case Typhoon Bolaven east of the Philippines, 18 Nov 2005. In (a-b), $T_{B_{89V}}$ and PCT_{89} were taken from AMSR-E Level 2A brightness temperatures distributed by NSIDC, because the level 1C XCAL files have values below 50 K set as missing. Comparison of nearby pixels slightly above 50 K suggests the calibrations are consistent within 1.0 K.

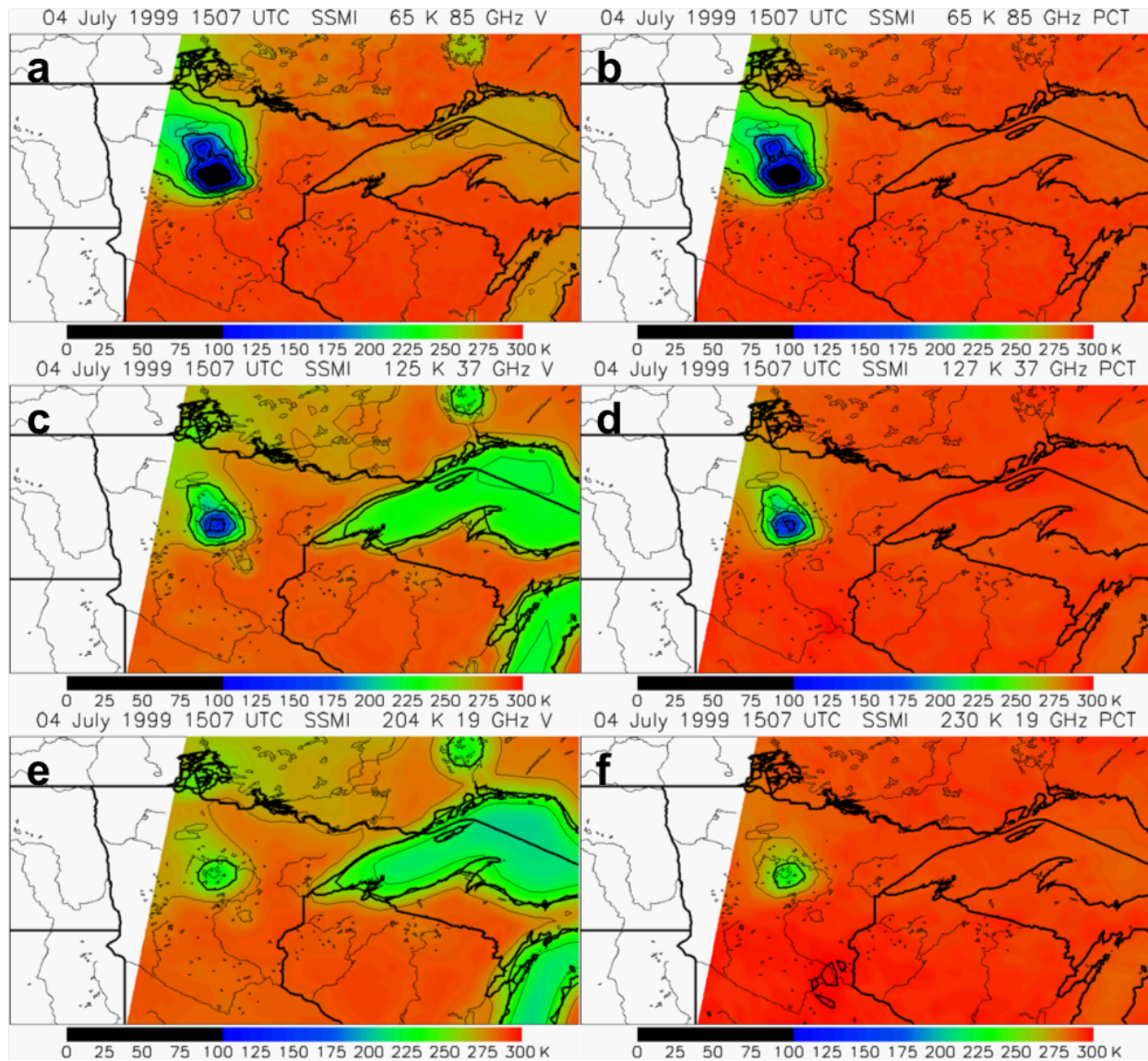


Figure 12. SSMI case from Minnesota, 04 July 1999. Left panels are vertically polarized brightness temperature, right columns are PCT. Contour interval 25 K, with thick contours every 50 K. The minimum brightness temperature (or PCT) in the domain is printed.